Low-energy plasmonic structure in CaC_6

J. P. Echeverry,[1,2] E. V. Chulkov,[1,2,3] P. M. Echenique,[1,2,3] and V. M. Silkin[1,2,4]

[1]*Donostia International Physics Center (DIPC), Paseo de Manuel Lardizabal 4, E-20018 San Sebastián, Basque Country, Spain*

[2]*Departamento de Física de Materiales, Facultad de Ciencias Químicas, Universidad del País Vasco (UPV-EHU), Apdo. 1072, E-20080 San Sebastián, Basque Country, Spain*

[3]*Centro de Física de Materiales (CFM), Materials Physics Center (MPC), Centro Mixto CSIC–UPV/EHU, Paseo de Manuel Lardizabal 5, E-20018 San Sebastián, Basque Country, Spain*

[4]*IKERBASQUE, Basque Foundation for Science, E-48011 Bilbao, Basque Country, Spain*

(Received 13 April 2012; published 22 May 2012)

The low-energy dielectric properties of CaC_6—a representative graphite intercalated compound (GIC)—were investigated by *ab initio* time-dependent density functional theory calculations with full inclusion of local field effects. The calculations predict the existence of several kinds of plasmons in CaC_6 with energy below 10 eV. The mode with the largest energy is a conventional "πp" mode strongly dispersing in the hexagonal basal plane and almost nondispersing in the perpendicular direction. In the 2.3–3 eV energy range, we find a long-lived intraband plasmon with negative (positive) dispersion with momentum transfer in (perpendicular to) the basal plane. In the 0–1.5 eV energy range, a mode with linear soundlike dispersion along all three high-symmetry directions is observed. All the three modes present strong anisotropy originated from the band structure. The physical origin of these excitation modes is discussed in terms of intra- and interband transitions. The crucial role of local field effects in the propagation of the two lowest-energy modes at large momentum transfers and in the determination of its dispersion over extended momentum-transfer region is analyzed.

DOI: 10.1103/PhysRevB.85.205135 PACS number(s): 71.45.Gm, 74.70.Wz

I. INTRODUCTION

By intercalation of graphite with some dopants, one can dramatically modify its physical properties.[1] In such process, in graphite, which is a semimetal and has a small concentration of electrons and holes at the Fermi level, the number of electronic states at the Fermi level can vary strongly. Considerable effort has been devoted to understand modifications in the electronic band structure accompanying the intercalation process such as the alteration of the carbon-derived energy bands and charge transfer processes from the foreign atoms to carbon planes.[2–4] In this respect, a special attention was directed to the evolution of a so-called interlayer band[5] of graphite, which being totally unoccupied in a pure graphite, can become partially occupied in some graphite-intercalated compounds (GICs).[6]

One of the important consequences of intercalation was the appearance of superconductivity in graphite doped with certain dopants, while pure graphite is not a superconductor. For years, this phenomenon attracts attention in spite of believing that the maximum critical temperature T_c was rather low. This subject attracted a renewed interest after the discovery of unusually high transition temperatures in the alkali-earth intercalated graphite compounds, YbC_6 and CaC_6, with T_c of 6.5 and 11.5 K, respectively.[7] Since this discovery, GICs became the subject of intensive studies in order to clarify the relevant mechanism behind this phenomenon. Nowadays, it is generally accepted that the BCS mechanism with conventional electron-phonon coupling[8,9] can explain the relatively high critical temperature T_c in these GICs. However, many interesting issues still remain open, especially, the relevance of different phonons groups in the electron-phonon coupling. Also, as was pointed out by Mazin *et al.*,[10] some inconsistences in the data obtained in measurements of isotope effect,[11] specific heat,[12–14] and others are awaiting a satisfactory solution.

On the other hand, soon after the discovery of enhanced T_c in YbC_6 and CaC_6 an interesting observation was made by Csányi *et al.* concerning the electronic structure of several superconducting and nonsuperconducting GICs.[6] They noted a correlation between an occupation of the interlayer energy band (which in pure graphite is totally unoccupied) and superconductivity, suggesting that the interlayer band plays a crucial role in the superconductivity phenomenon in these compounds. Based on this analysis, it was suggested that an electronic mechanism might be at the origin of superconductivity in that GICs where the interlayer band is partly occupied. In particular, it was suggested that since there are two kinds of carriers presented at the Fermi level in the energy bands (the carbon-derived π^* band and the interlayer band) a so-called acoustic plasmon (AP) could exist and play a role as a mediator, like phonons in the conventional BCS scenario.[15–18]

The collective electronic excitations, to the best of our knowledge, were neither investigated in YbC_6 nor in CaC_6. At the same time, there exist a rich literature[19–26] on this topic for other GICs. Thus in a variety of these compounds, modifications of the low-energy π plasmon mode existing in pure graphite at the 7–12 eV energy range were observed[27–29] resulting in a plasmon frequency shift to lower energies. Additionally, new features were also found in the excitation spectra of GICs like an intraband plasmon with frequency $\sim$1 eV. However, the existence of plasmonic modes at low energies that might be relevant for superconductivity has not been reported for any GIC.

The issue of existence of an AP in some GICs and, in particular, in CaC_6, was discussed in a number of publications. Mazin *et al.* suggested[10,30] that AP can not exist in CaC_6 arguing that in this compound, neither the effective masses of distinct energy bands are very different nor these bands are two-dimensional like. Hence neither of the two types[15–18,31–34] of AP, could exist in CaC_6.

On the other hand, in recent inelastic neutron and x-ray scattering experiments,[35,36] an unexpected intensity due to an additional mode at about 11 meV was detected that could be linked to the modified AP mode. However, from *ab initio* calculations, it was concluded that this mode cannot be attributed to the AP-like mode and alternative explanations of the origin of this mode as being an impurities mode[35] or due to polycrystalline nature of samples[36] were proposed.

At the same time, recent *ab initio* calculations[37,38] of the excitation spectra in bulk MgB_2 and Pd demonstrated that an AP can indeed exist in real materials. The crucial role of band structure in formation of a such mode was demonstrated. Moreover, in a layered material MgB_2, a peculiar "arclike" periodic dispersion of the acoustic mode was observed for momentum transfers in the direction perpendicular to the basal plane.

In the present work, we have studied collective electronic excitations in CaC_6 in the framework of time-dependent density functional theory in the 0–10 eV energy domain for momentum transfers in all three main symmetry directions. The calculations were performed with full inclusion of the *ab initio* energy band structure evaluated in a self-consistent pseudopotential scheme. Here, we analyze the relevance of different factors like local-field effects and exchange-correlation effects in the determination of the plasmonic structure of CaC_6 in this energy interval. In particular, we observe modifications in the energy position and dispersion of the π plasmon mode transforming to a truly three-dimensional feature, the appearance of an intraband plasmon with strongly anisotropic behavior, and report on the existence of a low-energy AP mode in all main symmetry momentum transfer directions. A crucial role of local-field effects in the transmittance of the last two modes at large momenta is demonstrated, while a minor role of exchange-correlation effects beyond the random phase approximation in this compound is established like in a pure graphite.[39] Note that this is a detailed *ab initio* investigation of the excitation spectra in CaC_6. In a previous attempt,[35] only the data for the *noninteracting* density response function calculated at one value of momentum transfer in a small energy window were reported.

This paper is organized as follows. In Sec. II, the formalism used and technical details of the calculations are described. In Sec. III, we present the CaC_6 band structure, the calculated dielectric function, and the energy-loss spectra for momentum transfers along main symmetry directions. Concluding remarks and the summary are presented in Sec. IV. Atomic units ($\hbar = e^2 = m_e = 1$) are used unless it is stated otherwise.

II. CALCULATION DETAILS

The CaC_6 compound crystalizes in the $R\bar{3}m$ structure forming an $A\alpha A\beta A\gamma$ stacking sequence in which all the graphite layers denoted by "A" have the same arrangement, while the calcium atoms occupy interlayer sites above the centers of carbon hexagons in an $\alpha\beta\gamma$ stacking. This lattice can be described using a rhombohedral basis in which a unit cell contains one calcium and six carbon atoms.[35] However, for convenience, in this work, we adopt a hexagonal basis in which the unit cell contains three chemical formula units. This unit cell and the corresponding first Brillouin zone (1BZ) are shown in Figs. 1(a) and 1(b), respectively. The definitions of the main symmetry directions in crystal and momentum transfers are given there as well. The experimental lattice parameters[36] of CaC_6, $a = 4.333$ Å and $c = 3\,c' = 13.572$ Å, were employed in present calculations. Here, c' is the distance between graphene layers.

We have calculated the band structure of CaC_6 within density functional theory describing the valence-core interaction of Ca and C by norm-conserving pseudopotentials.[40] The wave functions were expanded in the plane-wave basis

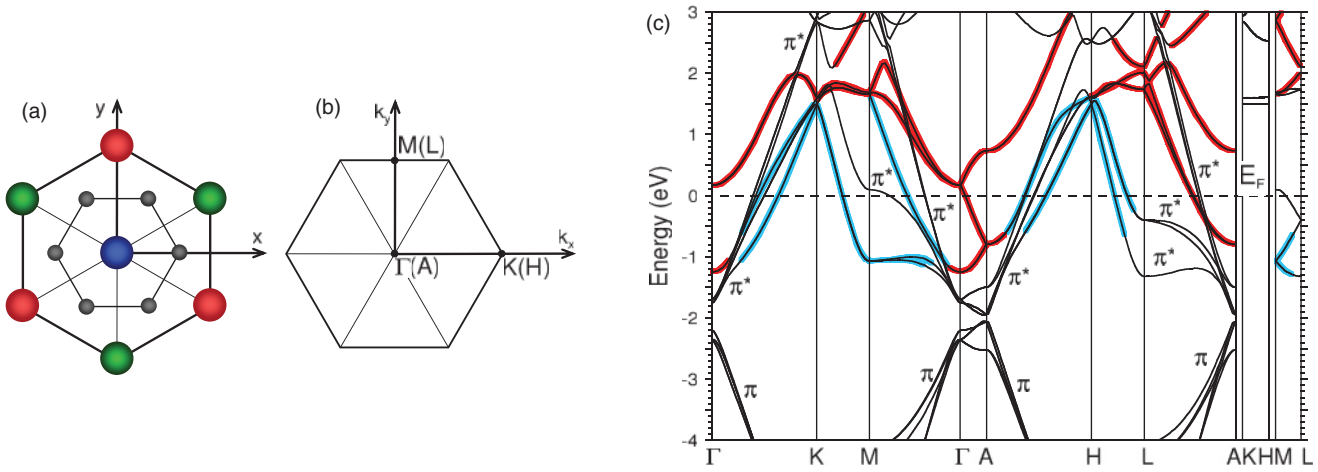

FIG. 1. (Color online) (a) Crystal structure of CaC_6 presented in the hexagonal basis and (b) the corresponding first Brillouin zone (1BZ). Positions of carbon atoms are shown by gray small dots and of calcium ions by large circles. All carbon layers have the same arrangement in the basal plane. The different colors for circles corresponding to the Ca atoms highlight three different calcium layers. In (b), the ΓKM and AHL planes cross the k_z axis, directed in direction perpendicular to the carbon basal plane, at $k_z = 0$ and $k_z = \pi/c$, respectively. Three main symmetry directions, a^*, b^*, and c^*, for the momentum transfers are directed along the ΓK, ΓM, and ΓA symmetry directions of the 1BZ, respectively. (c) Calculated band structure of CaC_6 along high-symmetry directions of the 1BZ. The interlayer and hybridized bands[6] are marked with red (dark) and blue (light) thick lines, respectively. The Fermi level located at the zero energy is shown by horizontal dashed line.

with an energy cutoff of 50 Ry. Self-consistent Kohn-Sham eigenvalues $\varepsilon_{n\mathbf{k}}$ and eigenfunctions $\psi_{n\mathbf{k}}(\mathbf{r})$ were obtained with the use of exchange-correlation potential of Ref. 41.

The calculated $\varepsilon_{n\mathbf{k}}$ and $\psi_{n\mathbf{k}}(\mathbf{r})$ were employed in the evaluation of the density response function for noninteracting electrons χ^o transformed to a matrix form in the reciprocal space:

$$\chi^o_{\mathbf{GG}'}(\mathbf{q},\omega) = \frac{2}{\Omega}\sum_{\mathbf{k}}^{1\mathrm{BZ}}\sum_{n,n'}\frac{(f_{n\mathbf{k}} - f_{n'\mathbf{k}+\mathbf{q}})\langle\psi_{n\mathbf{k}}|e^{-\mathrm{i}(\mathbf{q}+\mathbf{G})\cdot\mathbf{r}}|\psi_{n'\mathbf{k}+\mathbf{q}}\rangle\langle\psi_{n'\mathbf{k}+\mathbf{q}}|e^{\mathrm{i}(\mathbf{q}+\mathbf{G}')\cdot\mathbf{r}}|\psi_{n\mathbf{k}}\rangle}{\varepsilon_{n\mathbf{k}} - \varepsilon_{n'\mathbf{k}+\mathbf{q}} + (\omega + \mathrm{i}\eta)}. \quad (1)$$

Here, $\mathbf{q}$ and ω are momentum and energy, respectively. Factor 2 accounts for spin, Ω is a normalization volume, $\mathbf{G}$'s are the reciprocal lattice vectors, $f_{n\mathbf{k}}$ is the Fermi distribution function, and η a positive infinitesimal. The vector $\mathbf{q}$ is confined to the 1BZ and the sum in $\mathbf{k}$ is performed over the 1BZ.

In the framework of time-dependent density functional theory,[42,43] the density response function χ for interacting electrons is related to χ^o via the Dyson-like equation $\chi = \chi^o + \chi^o(\upsilon + K^{\mathrm{xc}})\chi$, which in a periodic crystal takes a matrix form:

$$\chi_{\mathbf{GG}'}(\mathbf{q},\omega) = \chi^o_{\mathbf{GG}'}(\mathbf{q},\omega) + \sum_{\mathbf{G}_1}\sum_{\mathbf{G}_2}\chi^o_{\mathbf{GG}_1}(\mathbf{q},\omega) \times\left[\upsilon_{\mathbf{G}_1}(\mathbf{q})\delta_{\mathbf{G}_1\mathbf{G}_2} + K^{\mathrm{xc}}_{\mathbf{G}_1\mathbf{G}_2}(\mathbf{q},\omega)\right]\chi_{\mathbf{G}_2\mathbf{G}'}(\mathbf{q},\omega). \quad (2)$$

In Eq. (2), $\upsilon_{\mathbf{G}_1}(\mathbf{q})$ is the Fourier transform of the bare Coulomb potential υ, and $K^{\mathrm{xc}}_{\mathbf{GG}'}(\mathbf{q},\omega)$ accounts for dynamical exchange-correlation effects. In this work, we present results obtained within the random-phase approximation (RPA) in which K^{xc} is set to zero. We checked that the use of a so-called adiabatic local density approximation (ALDA)[42,44] for K^{xc} does not change the excitation spectra in this compound significantly, in line with what was observed in the pure graphite case.[39]

The energy-loss function, $-\mathrm{Im}[\epsilon^{-1}_{\mathbf{GG}'}(\mathbf{q},\omega)]$, which is proportional to the dynamical structure factor $S(\mathbf{Q},\omega) \sim -\mathrm{Im}[\epsilon^{-1}_{\mathbf{GG}}(\mathbf{q},\omega)]$ (where $\mathbf{G} = \mathbf{Q} - \mathbf{q}$) directly probed in the inelastic x-ray and electron scattering experiments is given in terms of the density-response function, χ, by the equation

$$\epsilon^{-1}_{\mathbf{GG}'}(\mathbf{q},\omega) = \delta_{\mathbf{GG}'} + \upsilon_{\mathbf{G}}(\mathbf{q})\chi_{\mathbf{GG}'}(\mathbf{q},\omega). \quad (3)$$

The Fourier coefficients $\chi^0_{\mathbf{GG}'}(\mathbf{q},\omega)$ can be calculated numerically with the use of several methods.[45–52] The approach we adopt here consists[46,49] in the evaluation, at the first step, of the spectral function $S^0_{\mathbf{GG}'}(\mathbf{q},\omega)$ directly related to the imaginary part of $\chi^0_{\mathbf{GG}'}(\mathbf{q},\omega)$. In this case, instead of η, a relevant numerical parameter is a broadening parameter[37,46] γ which was set here to 10 meV. The sum over the 1BZ in Eq. (1) was performed with the use of a $48 \times 48 \times 18$ grid and all the energy bands up to energy of 50 eV above the Fermi level were included. Subsequently, once having the imaginary part evaluated, the real part of $\chi^0_{\mathbf{GG}'}(\mathbf{q},\omega)$ is obtained via the Hilbert transform using an energy cutoff of 50 eV. In the Fourier expansion of the χ^0, χ, and ϵ matrices 100 reciprocal vectors $\mathbf{G}$ were employed. Local field effects[53,54] are included in the evaluation of the energy-loss function through inclusion in Eq. (2) of the nondiagonal matrix elements.

III. CALCULATION RESULTS AND DISCUSSION

Figure 1(c) shows the calculated band structure of CaC_6 around the Fermi level along the high-symmetry directions of the 1BZ, which is in good agreement with previous first-principles calculations.[6,30,42,55] It is seen in the figure that intercalation of Ca atoms produces a downward shift of the carbon-derived bands by ~2 eV and the appearance of three kinds of bands at the Fermi level. The energy bands crossing the Fermi level in CaC_6 are the antibonding carbon-derived π^* band, the interlayer band, and the hybridized π^* band with strong charge density in the interlayer region.[6] In Fig. 1(c), these bands are highlighted by π^* symbols, red lines, and blue lines, respectively.

The dispersion of the π and π^* bands is slightly affected by the presence of the intercalant. The most strong modification in comparison with a pure graphite case is the formation of an energy gap of about 0.5 eV at the Γ point (a back-folded K point in the 1BZ of graphite).

The interlayer band has a parabolic-like dispersion at E_F in all three symmetry direction. The bottom of this band is located at −1.25 eV at the Γ point and at the A point its energy is of 0.7 eV. The hybridized bands are originated from the π^* bands of graphite whose dispersion is notably modified by the presence of Ca atoms. In particular, they present a rather strong dispersion at the Fermi level in the direction perpendicular to the graphene sheets as can be observed in Fig. 1(c) along the ML symmetry direction. Thus, in CaC_6, there exist three kinds of energy bands at the Fermi level with different Fermi velocities, a fact which has profound impact on the low-energy excitation spectra as it is shown below.

The calculated excitation spectra in CaC_6 are presented in Figs. 2–4. In these figures, the panels labeled as (a) and (b) show the loss function $-\mathrm{Im}[\epsilon^{-1}(\mathbf{Q},\omega)] \equiv -\mathrm{Im}[\epsilon^{-1}_{\mathbf{GG}}(\mathbf{q},\omega)]$ as a function of momentum transfer Q and energy ω with full inclusion and without inclusion of the LFEs, respectively. Note that the magnitude of the vector $\mathbf{Q}$ can exceed the size of the 1BZ since $\mathbf{Q} = \mathbf{q} + \mathbf{G}$. The panels (c) in the figures present the imaginary part of the corresponding dielectric function ϵ.

In Figs. 2(a), 3(a), and 4(a), one can see that CaC_6 has a rich spectrum with many spectral features. From comparison of Figs. 2 and 3 with Fig. 4, one can see that the spectral features and their evolution in the a^*-b^* plane and perpendicular to this plane (along the c^* axis) are very different suggesting strongly anisotropic dielectric properties of CaC_6. For momentum transfers in the a^*-b^* plane, we observe a rather isotropic plasmonic structure, although some quantitative differences can be detected.

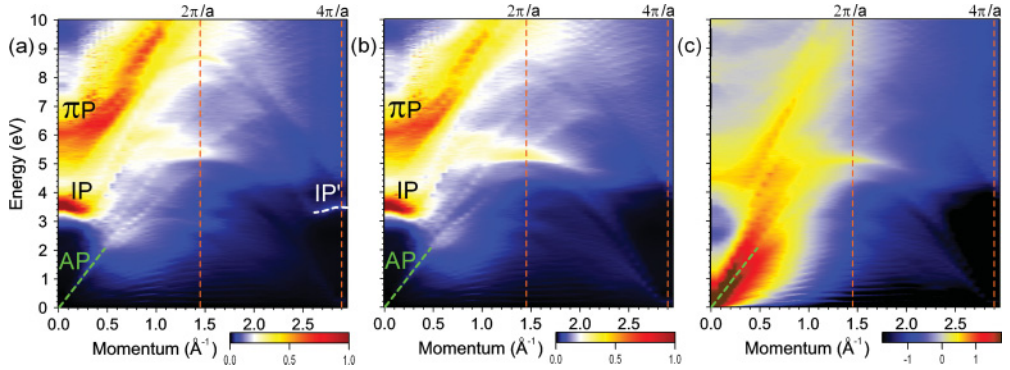

FIG. 2. (Color online) Loss function, $-\mathrm{Im}[\epsilon^{-1}(\mathbf{Q},\omega)]$, of CaC_6 calculated for momentum transfers $\mathbf{Q}$ along the a^* axis with (a) and without (b) inclusion of local-field effects. Calculations are performed with the RPA kernel. (c) Imaginary part of the corresponding dielectric function, $\log_{10}(\mathrm{Im}[\epsilon])$. The peaks corresponding to π plasmon (πP), intraband plasmon (IP), and acoustic plasmon (AP) are shown by the corresponding symbols. In (a), a peak corresponding to an intraband plasmon reappearing at large momenta is highlighted by white dashed line and denoted as IP′. In each panel, the AP dispersion is denoted by green dashed lines.

In Figs. 2(a) and 3(a), we can distinguish in the upper-energy region a broad peak labeled as "πp" showing a strong parabolic-like positive dispersion with the momentum transfer increase. The energy of this peak is of 6.1 eV at small Q's and the peak disperses up to ∼12 eV at large Q's. This feature can be classified as a conventional π plasmon also presented in pristine graphite at $\omega_{\pi p} \approx 7$ eV[19,20,39,56] and in the GICs at lower energies.[19–25] The redshift of the πp plasma frequency in CaC_6 in comparison with the plasmon frequency in pure graphite can be explained by the presence of a broad peak centered at 4.6 eV at small Q's in the imaginary part of ϵ seen in Figs. 2(c) and 3(c). As illustrated in Fig. 5, the presence of this local peak in $\mathrm{Im}[\epsilon]$ makes the real part of ϵ to reach zero at energies around 5 eV. As a result a broad peak centered at 6.1 eV appears in the loss function. From comparison of panels (a) with panels (b) in Figs. 2 and 3, one can see that the LFEs have small impact in this mode at all momenta and only subtle changes can be detected.

On the other hand, as seen in Fig. 4(a), the corresponding mode is completely different for momentum transfers along the c^* axis. Here, the πp mode is located at ∼5.2 eV at small Q's. Its lower energy in comparison with the a^*-b^* plane case can be explained by the presence of a stronger and broader interband peak in $\mathrm{Im}[\epsilon]$ at the 3–5 eV energy region. As a result, the real part of ϵ does not reach zero at ∼5 eV as can be seen in the data for $Q_{\|c^*} = 0.129$ Å^{-1} presented in Fig. 6. The resulting peak in the loss function corresponding to the πp mode is not as strong as for $\mathbf{Q}$'s laying in the a^*-b^* plane. In all three directions for momentum transfers, the peaks corresponding to this mode are rather broad, i.e., this mode is significantly damped and quickly decays into electron-hole pairs. Note, that in pure graphite such a mode does not exist at small $Q_{\|c^*}$'s[56,57] and appears along the c^* direction only at finite momenta with an oscillating dispersion with energy around $\omega \approx 4$ eV.[58] An interesting feature of this mode in CaC_6 is its reappearance, as a $\pi p'$ mode, at large momentum transfers along the c^* direction due to LFEs, as can be deduced from comparison of the calculated loss function in Figs. 4(a) and 4(b).

We interpret the next feature appearing in the a^*-b^* plane at lower energies as an intraband plasmon (IP) mode. It is a narrow sharp peak showing the highest intensity in the plane, dispersing negatively [going to lower energy values as $Q_{\|a^*}$ ($Q_{\|b^*}$) increases] from 3.5 eV at small Q's to around 3.3 eV (3.2 eV) at momentum transfers $Q_{\|a^*} \approx 0.5$ Å^{-1} ($Q_{\|b^*} \approx 0.45$ Å^{-1}). The relatively thin width of the IP peak

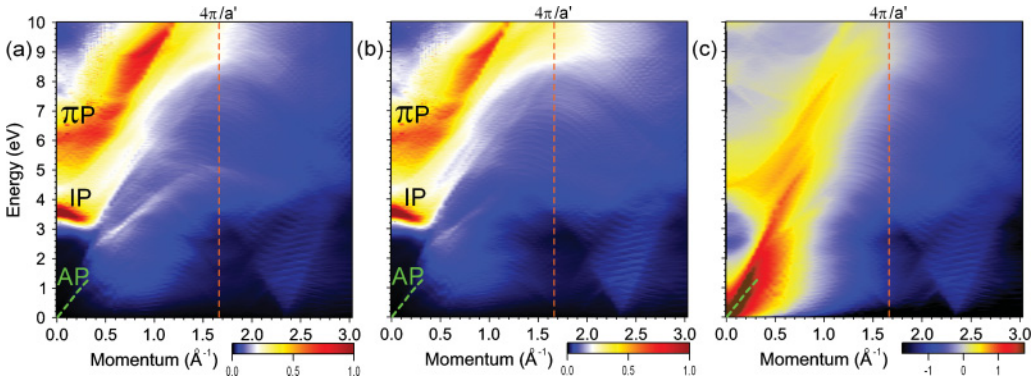

FIG. 3. (Color online) Loss function, $-\mathrm{Im}[\epsilon^{-1}(\mathbf{Q},\omega)]$, of CaC_6 calculated for momentum transfers $\mathbf{Q}$ along the b^* axis with (a) and without (b) inclusion of local-field effects. Calculations are performed with the RPA kernel. (c) Imaginary part of the corresponding dielectric function, $\log_{10}(\mathrm{Im}[\epsilon])$. The peaks corresponding to π plasmon (πP), intraband plasmon (IP), and acoustic plasmon (AP) are shown by the corresponding symbols. In each panel, the AP dispersion is denoted by green dashed lines. Here, $a' = a\sqrt{3}$.

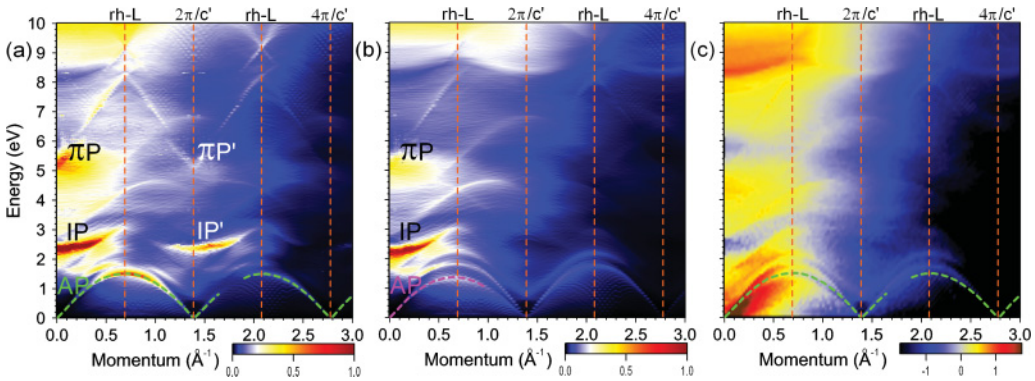

FIG. 4. (Color online) Loss function, $-\mathrm{Im}[\epsilon^{-1}(\mathbf{Q},\omega)]$, of CaC_6 calculated for momentum transfers $\mathbf{Q}$ along the c^* axis with (a) and without (b) inclusion of local-field effects. Calculations are performed with the RPA kernel. (c) Imaginary part of the corresponding dielectric function, $\log_{10}(\mathrm{Im}[\epsilon])$. The peaks corresponding to π plasmon (πP), intraband plasmon (IP), and acoustic plasmon (AP) are shown by the corresponding symbols. In (a), the peaks corresponding to the π plasmon and the intraband plasmon reappearing at large momenta are denoted as $\pi p'$ and IP′, respectively. The AP dispersion and its subsequent arclike dispersion is denoted by green dashed line. The same line is deposited in (c) as well. In (b), pink dashed line shows the AP dispersion and its subsequent transforation to electron-hole peak originated from the peak in $\mathrm{Im}[\epsilon]$. Here, points denoted as "rh-L" correspond to the L point in the BZ in the rhombohedral basis.

can be explained by the fact that it disperses in an energy gap between regions with strong intraband and interband transitions in $\mathrm{Im}[\epsilon]$ as can be appreciated in Figs. 2(c) and 3(c). Once this peak reaches the border of intraband electron-hole (e-h) continuum, it becomes heavily Landau-damped and disappears. The negative dispersion of this mode can be explained by the shape of the lower border of the region for interband transitions located at 4 eV at $Q = 0$ and dispersing downward with momentum increase along both the a^* and b^* directions as seen in Figs. 2(c) and 3(c). Thus, in the particular case of CaC_6, the negative dispersion of the IP mode can be explained by pure band structure effects. We are not aware of whether or not such negative dispersion of the IP mode has been reported previously in the GICs. However, a negative dispersion of an IP mode in other layered material like potassium-doped picene was recently observed and explained on base of competition between metallicity and electronic localization.[59] In several other layered compounds like transition-metal dichalcogenides, similar behavior of this mode was observed experimentally and an explanation for this phenomenon that goes beyond band structure effects was proposed.[60]

For momentum transfers along the c^* axis the corresponding IP mode is located at significantly lower energies as seen in Fig. 4(a), namely, at 2.35 eV for $Q_{\|c^*} = 0$. In this direction, the IP peak is sharp and has a linewidth of around 220 meV that corresponds to the lifetime of 3 fs. Contrary to what occurs in the a^*-b^* plane, the IP mode along the c^* axis has positive dispersion like in the MgB_2 layered compound.[61,62] In particular case of CaC_6, this positive dispersion can be explained by the shape of the gap in $\mathrm{Im}[\epsilon]$ where this mode disperses. In Fig. 4(c), it is seen that both the lower (at 1.7 eV at $Q_{\|c^*} = 0$) and the upper (at 2.7 eV at $Q_{\|c^*} = 0$) borders of this gap disperse upward with fairly the same slope up to

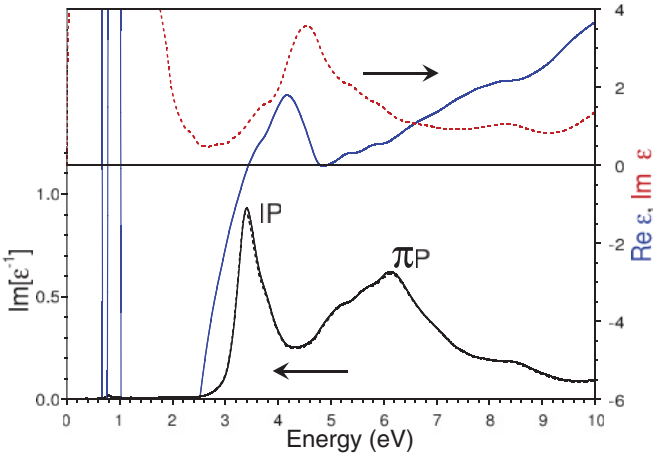

FIG. 5. (Color online) (Top) The real (blue solid line) and imaginary (red dashed line) parts of the calculated dielectric function at $Q_{\|a^*} = 0.181$ Å^{-1}. (Bottom) Corresponding loss function, $\mathrm{Im}[\epsilon^{-1}]$. Solid (dashed) line shows $\mathrm{Im}[\epsilon^{-1}]$ obtained in the calculation with (without) inclusion of the local-field effects.

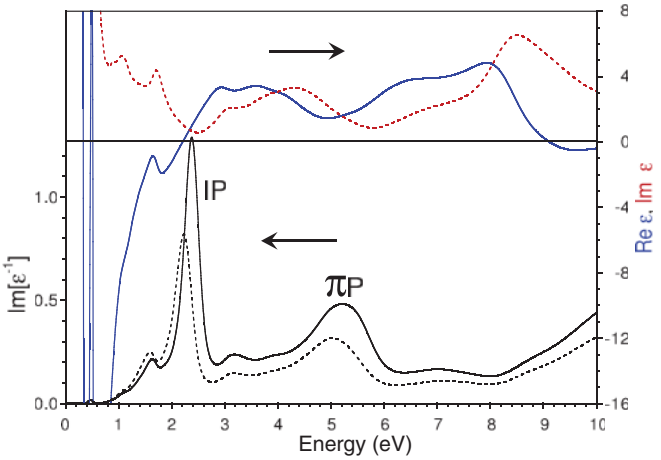

FIG. 6. (Color online) (Top) The real (blue solid line) and imaginary (red dashed line) parts of the calculated dielectric function at $Q_{\|c^*} = 0.129$ Å^{-1}. (Bottom) Corresponding loss function. Solid (dashed) line shows $\mathrm{Im}[\epsilon^{-1}]$ obtained in the calculation with (without) inclusion of the local-field effects.

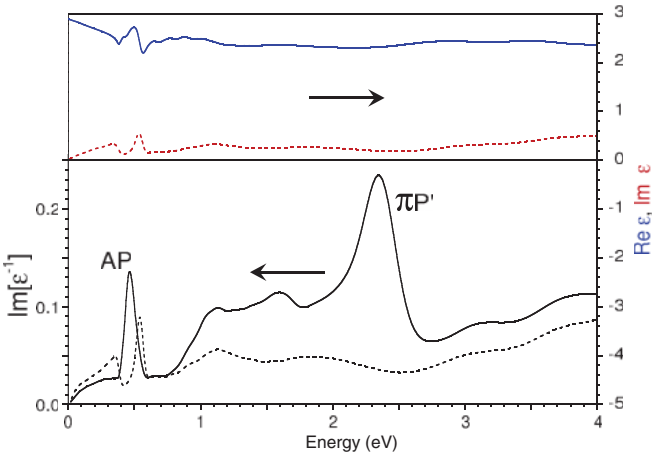

FIG. 7. (Color online) (Top) The real (blue solid line) and imaginary (red dashed line) parts of the calculated dielectric function at $Q_{\|c^*} = 1.26$ Å^{-1}. (Bottom) Corresponding loss function. Solid (dashed) line shows Im[ϵ^{-1}] obtained in the calculation with (without) inclusion of the local-field effects.

$Q = 0.5$ Å^{-1}. At larger momenta, the width of the gap gradually reduces and the IP mode gradually disappears accompanied also by gradual increase of e-h background in Im[ϵ] originated from interband transitions. Despite these residual transitions this mode can be clearly resolved up to $Q = 0.7$ Å^{-1}.

In contrast to what occurs with this mode in the b^* direction, along the a^* and c^* axes the IP mode reappears again upon momentum increase as one can see in Figs. 2(a) and 4(a) where we denote such a mode as IP′. The mechanism behind this effect is provided by the LFEs, as this feature does not appear when such effects are not included in the evaluation of the loss function as seen in Figs. 2(b) and 4(b). A more detailed picture is presented in Fig. 7 where the dielectric function and the corresponding loss function are shown at $Q_{\|c^*} = 1.26$ Å^{-1}. Here, one can see how when the LFEs are included a clear peak in the loss function appears at $\omega = 2.35$ eV, while when the LFEs are not included the loss function is featureless in this energy region due to featureless behavior of the imaginary and real parts of ϵ. Note how the IP′ peak starting from $Q = 2\pi/c' = 1.389$ Å^{-1} closely follows the dispersion of the IP mode. This phenomenon was in details explained for the cases of MgB_2,[63,64] graphite,[58] and compressed Li.[65] Note that the complete disappearance and subsequent reappearance of this mode with momentum transfer increase resembles the case of compressed lithium[65] and not the one of MgB_2 where continuous dispersion over subsequent BZ's is observed.[63,64]

In the low-energy range in Figs. 2(a) and 3(a), an additional feature in the loss function labeled AP can be detected. This feature disperses quasilinearly with momentum transfer and its energy seems to start from zero in the long-wave length (vanishing Q's) limit. It can be observed in the energy interval between 0 and ∼2.1 eV (∼1.2 eV) for momentum transfers along the a^* (b^*) axis. This dispersion corresponds to an AP mode recently predicted[37,38] to exist in Pd and MgB_2. However, it is for the first time that such kind of low-energy collective excitation is observed in a GIC system. In order to understand the origin of this mode, we show in Fig. 8 the real and imaginary parts of the dielectric function ϵ as well as the corresponding loss function evaluated at $Q_{\|a^*} = 0.181$ Å^{-1}. In the upper panel of the figure, one can see two main peaks in Im[ϵ], labeled as "IB" and "π^*," that have origin in the intraband transitions within the crossing the Fermi level interlayer and π^* bands, respectively. From a free-electron gas (FEG) theory[66] it is known that the intraband peak position in Im[ϵ] evaluated at a given Q is determined by the group velocities in the energy band crossing the Fermi level due to phase restrictions for electron-hole transitions imposed by denominator in Eq. (1). Moreover, the upper limit in energy for such transitions is determined by the maximal group velocity component in this momentum transfer direction (which in the isotropic FEG theory coincides with the maximal value of group velocity, although in general they can be different). However, in CaC_6, instead of one energy band, three kinds of energy bands cross the Fermi level as was discussed above. Figure 9 presents the calculated density of states (DOS) in these bands versus energy and the value of the corresponding group velocity component in all three main symmetry directions. In Figs. 9(a) and 9(b), one can observe at the Fermi level two main bands with distinct values for maximal group velocity components, $\upsilon_x^{F,\max}$ and $\upsilon_y^{F,\max}$. One group is characterized by $\upsilon_x^{F,\max}$ and $\upsilon_y^{F,\max}$ around 0.5 a.u., while the second is at 0.27 a.u. The former DOS corresponds to the π^* energy bands with strongest dispersion in the (a^*-b^*) plane observed in Fig. 1(c). In Figs. 9(a) and 9(b) it is seen how $\upsilon_x^{F,\max}$ and $\upsilon_y^{F,\max}$ reach the value of ∼0.4 a.u. at energies larger than the energy gap located at ∼−2 eV and after that gradually increase with energy increase reaching maximal values of 0.54 and 0.56 a.u. at ∼2 eV, respectively. The latter DOS is related to the interlayer band. One can see in Figs. 9(a) and 9(b) how $\upsilon_x^{F,\max}$ and $\upsilon_y^{F,\max}$ in this band quickly increases from zero at energy of −1.25 eV up to 0.27 at the Fermi level reaching maximum values of 0.33 a.u. at 1.5 eV and 0.35 at 1.2 eV, respectively. Some signature of the DOS in the hybridized band can be detected as a peak in the DOS at $\upsilon_x^{F,\max} = 0.4$ a.u. at the Fermi level.

The presence of carriers in different energy bands at the Fermi level with such different maximal group velocity components in the a^*-b^* plane produces two-intraband-peak structures in Im[ϵ], which indeed reflect a number of electron transitions in the system.[66] As a result, the real part of ϵ crosses the zero axis three times as demonstrated in Fig. 8. The first and third zero crossings coincide in energy with the local peaks in Im[ϵ] and, subsequently, no plasmonic peaks appear in the loss function at the corresponding energies. In contrast, the second zero crossing occurs at energy where Im[ϵ] has a local minimum and a well defined peak AP corresponding to the AP appears in the loss function at $\omega = 0.78$ eV. Hence the appearance of the AP mode in the a^*-b^* plane is a result of screening of the carriers in the interlayer band slowly moving in the basal plane by the carriers in the π^* bands moving faster in the same plane. Note that the presence of finite Im[ϵ] at energy where the AP peak appears does not destroy this mode as the linewidth of such a mode is determined by both Im[ϵ] and the Re[ϵ] energy derivative. As the d(Re[ϵ])/dω is large at this energy, a well defined peak is developed in the loss function. Since both intraband peaks in Im[ϵ] disperse

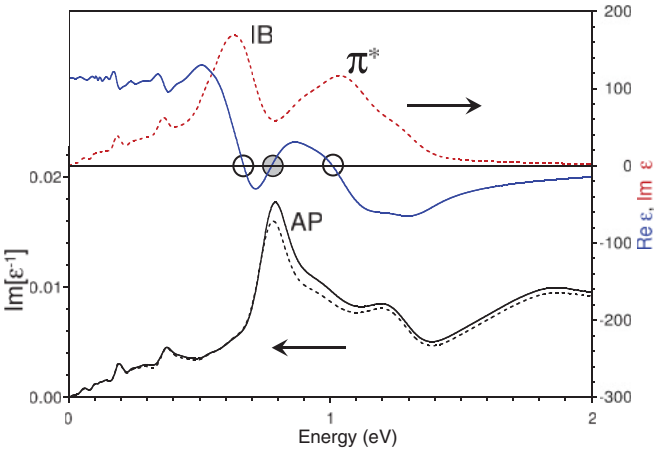

FIG. 8. (Color online) (Top) The real (blue solid line) and imaginary (red dashed line) parts of the dielectric function calculated for momentum transfer $Q_{\|a^*} = 0.181$ Å^{-1}. Peaks in Im[ϵ] labeled as "IB" and π^* are originated from the intraband transitions within the interlayer band and the π^* band, respectively. (Bottom) Corresponding loss function. Solid (dashed) line shows Im[ϵ^{-1}] obtained in the calculation with (without) inclusion of the local-field effects. The filled and empty circles highlights the zero crossings in Re[ϵ] leading and not leading, respectively, to the appearance of a plasmonic peak in the loss function.

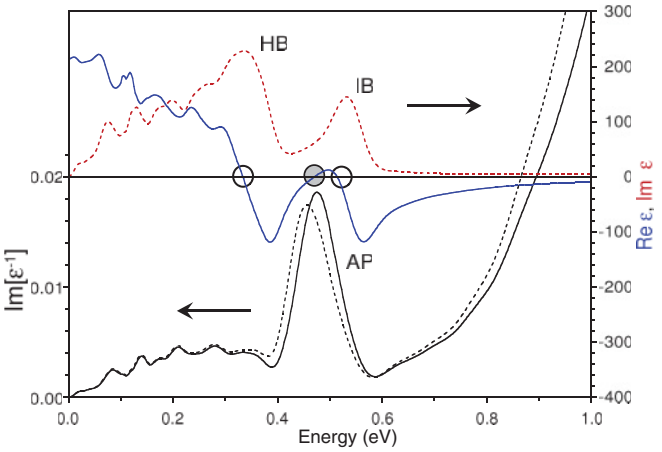

FIG. 10. (Color online) (Top) The real (blue solid line) and imaginary (red dashed line) parts of the calculated dielectric function at $Q_{\|c^*} = 0.129$ Å^{-1}. (Bottom) Corresponding loss function. Solid (dashed) line shows Im[ϵ^{-1}] obtained in the calculation with (without) inclusion of the local-field effects.

linearly with momentum, as can be observed in Figs. 2(c) and 3(c), the AP mode disperses linearly with momentum as well. From Figs. 2, 3, and 8, it is clear that the LFEs have minor impact on this mode. Upon momentum increase, the two-intraband-peak structure gradually loses its structure resulting in disappearance of the AP mode.

Inspection of the low-energy excitation spectra at momentum transfers along the c^* axis presented in Fig. 4 reveals that the loss function along this direction is quite different in comparison with that in the a^*-b^* plane. At small momenta, one can also see a well defined AP peak in the loss function corresponding to the AP mode. The origin of such a mode in this momentum direction is the same as for momentum transfers in the basal plane—the presence of several energy bands crossing the Fermi level with different group velocity components in this direction. However, as can be deduced from the analysis of the corresponding DOS in Fig. 9(c), here the situation is different. Now the maximal group velocity in this direction $v_x^{\max}$ is observed in the interlayer band. Thus, at the Fermi level, the velocity component reaches a value of 0.38 a.u. coming from the interlayer energy band along the ΓA direction of the 1BZ. The carriers with lower maximal group velocity in this direction reside in the hybridized band. For example, $v_z^{F,\max}$ is 0.2 a.u. for such carriers. In Fig. 9(c), one can see that even more number of states have very small group velocity in this direction. Nevertheless, we do not detect in the Im[ϵ] a separate structure corresponding to these states with extremely slow group velocity. Only some enhancement can be observed on the low-energy side of the lower-energy peak as can be seen in Fig. 10 where we present the dielectric function and corresponding loss function evaluated at $Q_{\|c^*} = 0.129$ Å^{-1}. On contrary, two clear peaks in Im[ϵ] labeled as "HB" and "IB" and corresponding to intraband transitions in the hybridized and the interlayer bands, respectively, can be seen in the same figure and on a more general scale in Fig. 4(c). Hence the AP mode at momentum transfers in the c^* direction can be understood as being a result of dynamical screening of the slower carriers in the hybridized band by the carriers in the interlayer band faster moving in this direction.

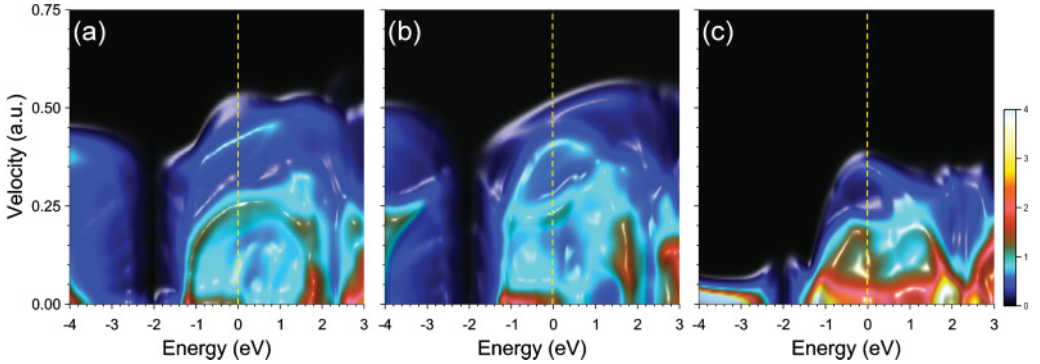

FIG. 9. (Color online) Maps of the density of states in energy bands in vicinity of the Fermi level in CaC_6 vs energy and group velocity components along (a) a^*, (b) b^*, and (c) c^* axes. The energies are relative to the Fermi level.

Following the AP peak dispersion in Fig. 4(a) in the c^* direction one observes that, contrary to what occurs in the a^*-b^* plane, its dispersion reaches the maximum energy of 1.5 eV at $Q_{\|c^*} = 0.694$ Å^{-1} and does not disappear. Instead, after reaching the maximum energy, the dispersion of this peak turns to be negative and reaches zero energy at $Q_{\|c^*} = 2\pi/c' = 1.389$ Å^{-1}, and after that acquires a positive dispersion again. That this behavior is a demonstration of the LFEs is confirmed by the fact that when they are not included in the evaluation of the loss function a similar peak in Im$[\epsilon^{-1}]$ can be traced up to $Q_{\|c^*} = 0.9$Å^{-1} only as seen in Fig. 4(b). Moreover, being at the small $Q_{\|c^*}$'s, a true AP peak its nature gradually changes to the simple e-h peak reflecting the enhanced Im$[\epsilon]$ at the same energy. This can be appreciated in Fig. 7 where the dielectric function and the loss function calculated at $Q_{\|c^*} = 1.26$ Å^{-1} are presented. Even if a peak at $\omega = 0.55$ eV is presented in the loss function calculated without inclusion of the LFEs, it can not be interpreted as a plasmon mode because there is no zero crossing in Re$[\epsilon]$ and Im$[\epsilon]$ has a local maximum at the same energy. Contrary, the AP peak in the loss function evaluated with inclusion of LFEs, is located at 0.47 eV, exactly where the AP peak appears at $Q_{\|c^*} = 0.129$ Å^{-1} (see Fig. 10). Note that the process is facilitated by the fact that at $Q_{\|c^*} = 1.26$ Å^{-1}, Im$[\epsilon]$ possesses a local minimum in this energy region.

This arclike dispersion of the lowest-energy plasmon mode for momentum transfers in the direction perpendicular to the basal plane was previously reported[38] only in the case of other layered material, MgB_2. However, as seen in Fig. 4(a), in CaC_6, the dispersion of this mode is not continuous and this mode disappears for certain momenta, whereas in MgB2 the corresponding mode disperses without breaking over the extended momentum transfers region.

IV. CONCLUSIONS

We have reported the results of *ab initio* calculations of the dynamical momentum-dependent dielectric response of CaC_6 at the 0–10 eV energy range. Calculations were performed within the RPA with full inclusion of local-field effects. Our results demonstrate that intercalation of calcium atoms strongly modifies the dielectric properties of graphite in this energy region leading to a notable change in the π plasmon and to the appearance of two additional low-energy modes.

In particular, the energy of the π mode is reduced up to 6.1 at small momentum transfers in the basal a^*-b^* plane and a corresponding mode appears at $\omega = 5.2$ eV in the perpendicular direction. An additional mode—intraband plasmon—appears in the 2.35–3.5 eV energy region and its dispersion is characterized by strong anisotropy, being negative in the basal plane like in some other layered materials[59,60] and positive in the perpendicular direction.

In the energy range from zero to ∼2 eV, we find another mode—acoustic-like plasmon—which in CaC_6, in difference to MgB_2, appears in all three symmetry directions. We explain this distinct behavior by the different Fermi velocities in three kinds of energy bands crossing the Fermi level in this compound. Thus, for momentum transfers in the basal plane, this mode corresponds to the collective motion of the fast carriers in the π^* band with respect to the slow ones in the interlayer band. In the perpendicular direction, the role of the fast and slow carriers are played by the ones in the interlayer band and hybridized band, respectively. It would be of great interest to quantify the possible role of the AP mode in the interelectron coupling in the CaC_6. However, this is outside of the scope of this work. Due to its soundlike dispersion, the AP at small energy can interact with the optical phonon modes in the similar way as was proposed[38] for MgB_2. However, to observe this interaction with lattice vibrations, one should performed measurements of phonon dispersions at rather small momentum transfers. On the other hand, the AP dispersion over extended range of momentum transfer can be measured in the energy-loss experiments. Up to now, this kind of mode was not observed in bulk metals, whereas a similar mode theoretically predicted to exist at some metal surfaces with partly occupied surface states, called an acoustic surface plasmon,[67,68] was recently observed on a variety of metal surfaces[69–71] and graphene-based systems.[72–74]

Present results demonstrate the important role of local-field effects in the formation of the low-energy excitation spectra and dielectric properties of CaC_6 at large momentum transfers, especially in the perpendicular direction. Thus, due to these effects, the π and intraband plasmon peaks reappear in the excitation spectra at momentum transfers close to the center of subsequent BZs in this direction. The role of LFEs is even more crucial in the determination of the AP dispersion, where peculiar arclike dispersion is formed. Note that a similar mode with arclike dispersion was predicted to exist in other superconducting material, MgB_2 in the 0–0.5 eV energy region and still it has not been detected experimentally. In our opinion, CaC_6 is a better candidate for observation of such a mode since in this compound the AP mode reaches energy as high as 1.5 eV at large momenta in the perpendicular direction. Moreover, in CaC_6, it is a truly 3D feature at small momentum transfers and therefore a corresponding signal might be stronger in comparison with MgB_2.

ACKNOWLEDGMENTS

We acknowledge partial support from the Basque Departamento de Educación, Universidades e Investigación (Grant No. IT-366-07), CONSOLIDER, and the Spanish Ministerio de Ciencia e Innovación (Grant No. FIS2010-19609-C02-00).

[1] M. S. Dresselhaus and G. Dresselhaus, Adv. Phys. **30**, 139 (1981).
[2] N. A. W. Holzwarth, S. Rabii, and L. A. Girifalco, Phys. Rev. B **18**, 5190 (1978).
[3] W. Eberhardt, I. T. McGovern, E. W. Plummer, and J. E. Fischer, Phys. Rev. Lett. **44**, 200 (1980).
[4] D. P. DiVincenzo and S. Rabii, Phys. Rev. B **25**, 4110 (1982).

[5]Note than in literature, different authors frequently use different names referring to this band: interlayer band, free-electron-like band, and even considering it as a trapped first image-potential state of graphene.[75] Upon metal intercalation, its analog is called an intercalant-derived band[30] as well. We agree with Mazin[30] that indeed the definition of the character of such kind of band and corresponding discussion are somewhat philosophical, and just for concreteness in the following will refer to this band as an interlayer band.

[6]G. Csányi, P. B. Littlewood, A. H. Nevidomskyy, C. J. Pickard, and B. D. Simons, Nat. Phys. **1**, 42 (2005).

[7]T. E. Weller, M. Ellerby, S. S. Saxena, R. P. Smith, and N. T. Skipper, Nat. Phys. **1**, 39 (2005).

[8]M. Calandra and F. Mauri, Phys. Stat. Solidi B **13**, 3458 (2006).

[9]Y. Takada, J. Supercond. Nov. Mag. **22**, 89 (2009).

[10]I. I. Mazin, L. Boeri, O. V. Dolgov, A. A. Golubov, G. B. Bachelet, M. Giantomassi, and O. K. Andersen, Physica C **460**, 116 (2007).

[11]D. G. Hinks, D. Rosenmann, H. Claus, M. S. Bailey, and J. D. Jorgensen, Phys. Rev. B **75**, 014509 (2007).

[12]M. P. M. Dean, A. C. Walters, C. A. Howard, T. E. Weller, M. Calandra, F. Mauri, M. Ellerby, S. S. Saxena, A. Ivanov, and D. F. McMorrow, Phys. Rev. B **82**, 014533 (2010).

[13]A. Sanna, G. Profeta, A. Floris, A. Marini, E. K. U. Gross, and S. Massidda, Phys. Rev. B **75**, 020511 (2007).

[14]J. S. Kim, R. K. Kremer, L. Boeri, and F. S. Razavi, Phys. Rev. Let. **96**, 217002 (2006).

[15]B. T. Geilikman, Usp. Fiz. Nauk **88**, 327 (1966) [Sov. Phys. Usp. **9**, 142 (1966)].

[16]E. A. Pashitski, Zh. Eksp. Teor. Fiz. **55**, 2387 (1968) [Sov. Phys. JETP **28**, 1267 (1969)].

[17]Y. A. Uspensky, Zh. Eksp. Teor. Fiz. **76**, 1620 (1979) [Sov. Phys. JETP **49**, 822 (1979)].

[18]H. Fröhlich, J. Phys. C **1**, 544 (1968).

[19]J. J. Ritsko and M. J. Rice, Phys. Rev. Lett. **42**, 666 (1979).

[20]D. M. Hwang, M. Utlaut, M. S. Isaacson, and S. A. Solin, Phys. Rev. Lett. **43**, 882 (1979).

[21]J. J. Ritsko and E. J. Mele, Phys. Rev. B **21**, 730 (1980).

[22]J. J. Ritsko, E. J. Mele, and I. P. Gates, Phys. Rev. B **24**, 6114 (1981).

[23]L. A. Grunes and J. J. Ritsko, Phys. Rev. B **28**, 3439 (1983).

[24]L. A. Grunes, I. P. Gates, J. J. Ritsko, E. J. Mele, D. P. DiVincenzo, M. E. Preil, and J. E. Fischer, Phys. Rev. B **28**, 6681 (1983).

[25]J. E. Fischer, J. M. Bloch, C. C. Shieh, M. E. Preil, and K. Jelley, Phys. Rev. B **31**, 4773 (1985).

[26]K. W.-K. Shung, Phys. Rev. B **34**, 979 (1986).

[27]E. A. Taft and H. R. Philipp, Phys. Rev. **138**, A197 (1965).

[28]W. Schülke, U. Bonse, H. Nagasawa, A. Kaprolat, and A. Berthold, Phys. Rev. B **38**, 2112 (1988).

[29]T. Pichler, M. Knupfer, M. S. Golden, J. Fink, A. Rinzler, and R. E. Smalley, Phys. Rev. Lett. **80**, 4729 (1998).

[30]I. I. Mazin, Phys. Rev. Lett. **95**, 227001 (2005).

[31]J. Ruvalds, Adv. Phys. **30**, 677 (1981).

[32]V. Z. Kresin and H. Morawitz, Phys. Rev. B **37**, 7854 (1988).

[33]R. F. Wood, B. E. Sernelius, and A. L. Chernyshev, Phys. Rev. B **66**, 014513 (2002).

[34]V. Z. Kresin and S. A. Wolf, Rev. Mod. Phys. **81**, 481 (2009).

[35]M. D'Astuto, M. Calandra, N. Bendiab, G. Loupias, F. Mauri, S. Zhou, J. Graf, A. Lanzara, N. Emery, C. Hérold, P. Lagrange, D. Petitgrand, and M. Hoesch, Phys. Rev. B **81**, 104519 (2010).

[36]A. C. Walters, C. A. Howard, M. H. Upton, M. P. M. Dean, A. Alatas, B. M. Leu, M. Ellerby, D. F. McMorrow, J. P. Hill, M. Calandra, and F. Mauri, Phys. Rev. B **84**, 014511 (2011).

[37]V. M. Silkin, I. P. Chernov, Yu. M. Koroteev, and E. V. Chulkov, Phys. Rev. B **80**, 245114 (2009).

[38]V. M. Silkin, A. Balassis, P. M. Echenique, and E. V. Chulkov, Phys. Rev. B **80**, 054521 (2009).

[39]A. G. Marinopoulos, L. Reining, V. Olevano, A. Rubio, T. Pichler, X. Liu, M. Knupfer, and J. Fink, Phys. Rev. Lett. **89**, 076402 (2002).

[40]N. Troullier and J. L. Martins, Phys. Rev. B **43**, 1993 (1991).

[41]D. M. Ceperley and B. J. Alder, Phys. Rev. Lett. **45**, 566 (1980); as parametrized by J. P. Perdew and A. Zunger, Phys. Rev. B **23**, 5048 (1981).

[42]E. Runge and E. K. U. Gross, Phys. Rev. Lett. **52**, 997 (1984).

[43]M. Petersilka, U. J. Gossmann, and E. K. U. Gross, Phys. Rev. Lett. **76**, 1212 (1996).

[44]E. K. U. Gross and W. Kohn, Phys. Rev. Lett. **55**, 2850 (1985).

[45]N. E. Maddocks, R. W. Godby, and R. J. Needs, Europhys. Lett. **27**, 681 (1994).

[46]F. Aryasetiawan and O. Gunnarsson, Phys. Rev. B **49**, 16214 (1994).

[47]W. Ku and A. G. Eguiluz, Phys. Rev. Lett. **82**, 2350 (1999).

[48]E. E. Krasovskii and W. Schattke, Phys. Rev. B **60**, R16251 (1999).

[49]F. Aryasetiawan, in *Strong Coulomb Correlations in Electronic Structure Calculations*, edited by V. I. Anisimov (Gordon and Beach, Singapore, 2001).

[50]V. P. Zhukov, F. Aryasetiawan, E. V. Chulkov, and P. M. Echenique, Phys. Rev. B **65**, 115116 (2002).

[51]V. P. Zhukov, E. V. Chulkov, and P. M. Echenique, Phys. Rev. Lett. **93**, 096401 (2004).

[52]R. Díez Muiño, D. Sánchez-Portal, V. M. Silkin, E. V. Chulkov, and P. M. Echenique, Proc. Natl. Acad. Sci. USA **108**, 971 (2011).

[53]S. L. Adler, Phys. Rev. **126**, 413 (1962).

[54]N. Wiser, Phys. Rev. **129**, 62 (1963).

[55]M. Calandra and F. Mauri, Phys. Rev. B **74**, 094507 (2006).

[56]A. G. Marinopoulos, L. Reining, A. Rubio, and V. Olevano, Phys. Rev. B **69**, 245419 (2004).

[57]N. Barrett, E. E. Krasovskii, J.-M. Themlin, and V. N. Strocov, Phys. Rev. B **71**, 035427 (2005).

[58]R. Hambach, C. Giorgetti, N. Hiraoka, Y. Q. Cai, F. Sottile, A. G. Marinopoulos, F. Bechstedt, and L. Reining, Phys. Rev. Lett. **101**, 266406 (2008).

[59]P. Cudazzo, M. Gatti, F. Roth, B. Mahns, M. Knupfer, and A. Rubio, Phys. Rev. B **84**, 155118 (2011).

[60]J. van Wezel, R. Schuster, A. König, M. Knupfer, J. van den Brink, H. Berger, and B. Büchner, Phys. Rev. Lett. **107**, 176404 (2011).

[61]V. P. Zhukov, V. M. Silkin, E. V. Chulkov, and P. M. Echenique, Phys. Rev. B **64**, 180507(R) (2001).

[62]W. Ku, W. E. Pickett, R. T. Scalettar, and A. G. Eguiluz, Phys. Rev. Let. **88**, 057001 (2002).

[63]Y. Q. Cai, P. C. Chow, O. D. Restrepo, Y. Takano, K. Togano, H. Kito, H. Ishii, C. C. Chen, K. S. Liang, C. T. Chen, S. Tsuda, S. Shin, C. C. Kao, W. Ku, and A. G. Eguiluz, Phys. Rev. Lett. **97**, 176402 (2006).

[64]A. Balassis, E. V. Chulkov, P. M. Echenique, and V. M. Silkin, Phys. Rev. B **78**, 224502 (2008).

[65]I. Errea, A. Rodriguez-Prieto, B. Rousseau, V. M. Silkin, and A. Bergara, Phys. Rev. B **81**, 205105 (2010).

[66]D. Pines and P. Nozières, *The Theory of Quantum Liquids* (Benjamin, New York, 1966), Vol. 1.
[67]V. M. Silkin, A. García-Lekue, J. M. Pitarke, E. V. Chulkov, E. Zaremba, and P. M. Echenique, Europhys. Lett. **66**, 260 (2004).
[68]V. M. Silkin, J. M. Pitarke, E. V. Chulkov, and P. M. Echenique, Phys. Rev. B **72**, 115435 (2005).
[69]B. Diaconescu, K. Pohl, L. Vattuone, L. Savio, Ph. Hofmann, V. M. Silkin, J. M. Pitarke, E. V. Chulkov, P. M. Echenique, D. Farías, and M. Rocca, Nature (London) **448**, 57 (2007).
[70]S. J. Park and R. E. Palmer, Phys. Rev. Lett. **105**, 016801 (2010).
[71]K. Pohl, B. Diaconescu, G. Vercelli, L. Vattuone, V. M. Silkin, E. V. Chulkov, P. M. Echenique, and M. Rocca, Europhys. Lett. **90**, 57006 (2010).
[72]H. Pfnür, T. Langer, J. Baringhaus, and C. Tegenkamp, J. Phys.: Condens. Matter **23**, 112204 (2011).
[73]A. Politano, A. R. Marino, V. Formoso, D. Farías, R. Miranda, and G. Chiarello, Phys. Rev. B **84**, 033401 (2011).
[74]T. Langer, D. F. Föster, C. Bussi, T. Michely, H. Pfnür, and C. Tegenkamp, New J. Phys. **13**, 053006 (2011).
[75]V. M. Silkin, J. Zhao, F. Guinea, E. V. Chulkov, P. M. Echenique, and H. Petek, Phys. Rev. B **80**, 121408(R) (2009).